Reducing the corrosion rate of magnesium alloys using ethylene glycol for advanced electrochemical imaging

CrossMark

R. Matthew Asmussen [a], W. Jeffrey Binns [a], Pellumb Jakupi [a], Philippe Dauphin-Ducharme [b], Ushula M. Tefashe [b], Janine Mauzeroll [b], David Shoesmith [a,*]

[a] Department of Chemistry and Surface Science Western, University of Western Ontario, London, ON, Canada
[b] Department of Chemistry, McGill University, Montreal, QC, Canada

ARTICLE INFO

ABSTRACT

The corrosion of an AM50 Mg alloy was studied in ethylene glycol using electrochemical and electron microscopy techniques. Switching from H_2O to ethylene glycol, it was shown that the corrosion of the AM50 alloy was significantly suppressed thereby slowing H_2 evolution. The corrosion of the AM50 alloy was mapped using scanning electrochemical microscopy in the feedback mode. Ferrocenemethanol can be used to expose the reactive anodic areas on the Mg alloy. These studies confirmed that studies in ethylene glycol can be used to elucidate reaction features obscured by rapid corrosion in H_2O without significantly altering the mechanism and damage morphology.

Crown Copyright © 2015 Published by Elsevier Ltd. All rights reserved.

1. Introduction

Mg alloys possess several desirable properties for use in the automotive and aerospace industries, such as their high strength to weight ratio and good castability [1]. A deterrent to their application is their high corrosion rates in aqueous media. Driving the corrosion of Mg alloys is the microgalvanic coupling between the α-Mg matrix and the secondary microstructural constituents, such as β-phase and intermetallic particles [2] with the cathodic reactivity of the latter increased if it contains contaminant elements such as Fe [3]. Understanding the behavior of these microstructural features during corrosion is essential if alloys with improved corrosion properties are to be developed. Separating the responses of individual microstructural components acting as cathodes is inherently difficult using standard electrochemical measurements.

Scanning probe techniques provide valuable insights on a microscale with high spatial resolution. Such techniques have been applied to study the corrosion of Mg alloys including localized electrochemical impedance spectroscopy (LEIS) [4,5], scanning Kelvin probe force microscopy (SKPFM) [6,7], the scanning vibrating electrode (SVET) technique [8–12], and different modes of scanning electrochemical microscopy (SECM) [13–17]. Monitoring

corrosion processes above Mg alloys in an aqueous environment with these techniques is challenging because of large H_2 fluxes evolving as corrosion progresses which can interfere with mediator detection at the microelectrode tip and create a convective medium at the corroding surface [18]. Recently, these fluxes of H_2 have been used to monitor the corrosion process on Mg alloys [19,20].

To overcome this issue we have focused on controlling the corrosion rate, and hence, the amount of H_2 produced, using ethylene glycol as the corrosion medium since it limits the availability of H_2O, the primary cathodic reagent during corrosion. The corrosion of Mg alloys in ethylene glycol solutions has previously been investigated with a primary focus on their behavior as potential engine block materials which use ethylene glycol-based coolants [21–23]. In these studies increasing the ratio of ethylene glycol to H_2O was found to decrease the corrosion rate of the Mg alloys, although little detail was paid to pure ethylene glycol or to this solvent containing only small percentages of H_2O. Corrosion was also not investigated on the microscale.

Here, we present a study of the corrosion of the AM50 Mg alloy in ethylene glycol using a range of electrochemical techniques, including SECM, to compare the corrosion behavior to that observed in aqueous solution. Scanning electron microscopy (SEM) and energy dispersive X-ray analyses (XEDS) were used to locate and elementally analyze the alloy microstructure, and to locate and correlate surface microstructural features with an *in-situ* SECM map. Confocal scanning laser microscopy (CLSM) was used to observe the locations of corrosion damage.

---

* Corresponding author at: Western University, 1161 Richmond St. London, ON N6A 5B7, Canada. Tel.: +1 519 661 2111x86366.
  E-mail address: dwshoesm@uwo.ca (D. Shoesmith).

2. Experimental procedures

2.1. Materials

Bulk AM50 sand cast and graphite cast Mg alloy rods were received from General Motors Canada and machined into 1 cm × 1 cm × 0.7 cm size samples. For SECM measurements the AM50 sand cast alloy was machined into 4 mm × 4 mm × 0.5 cm samples. All samples were threaded on the backside to allow connection to external circuitry, and Struers EpoFix epoxy resin was used to seal the samples allowing only the exposure of a single face to the aqueous solution. Solutions were prepared with ethylene glycol (ACP), reagent grade NaCl (Caledon), ferrocenemethanol (FcMeOH) (97% Sigma Aldrich Canada), and NanoPure® (18.2 MΩ cm) H_2O.

2.2. Sample preparation

The mounted AM50 samples were ground successively with 800, 1200, 2400 grit SiC paper with a 50:50 ethanol/isopropanol solution as a lubricant, and subsequently polished with a Struers DP-Dur cloth saturated in 3 μm Struers DP-Suspension A for 5–10 min with the ethanol/propanol mixture once again used as a lubricant. A final 2–3 min polish was performed on a Struers OP-Chem cloth using an equal volume mixture of Struers OP-S Suspension and ethylene glycol, as an abrasive. The polished sample was then rinsed and sonicated in anhydrous ethanol for 2 min, Ar dried, and stored in a desiccator.

2.3. Electrochemical measurements

Electrochemical measurements were carried out in a standard three electrode cell with a Pt-mesh counter electrode and a saturated calomel reference electrode (SCE) (with a Luggin capillary placed 2 mm from the working electrode) in aerated solutions at ~22 °C. Electrochemical responses were measured with a Solartron® 1287 potentiostat coupled to a Solartron® 1255B frequency response analyzer for electrochemical impedance spectroscopy (EIS) measurements.

For corrosion potential (E_{CORR}) measurements the samples were placed in solution, face down for selected durations. Potentiodynamic polarization (PDP) scans were performed following a 2 h exposure to solution by scanning (at 0.167 mV/s) from −200 mV below E_{CORR} to either −800 mV (vs. SCE), or until a current density of 0.05 mA/cm² was measured to limit the extent of surface damage to the sample. EIS measurements were performed by potentiostatically fixing the potential and applying a sinusoidal potential perturbation of ±10 mV vs. E_{CORR}. The current response was recorded over the frequency range, 10^5 Hz to 10^{-3} Hz, and a one point per decade reverse scan was recorded from 10^{-2} to 10^5 Hz to ensure steady-state was maintained throughout the measurement.

2.4. Electron microscopy

Scanning electron microscopy (SEM) images were collected in secondary electron (SE) and back scattered electron (BSE) modes on either a LEO 440, Hitachi 3400-N Variable Pressure SEM, LEO 1540 XB SEM, or a Hitachi SU6600 Field Emission SEM. X-ray energy dispersive spectroscopy (XEDS) maps were collected using a Quartz XOne XEDS system. Confocal laser scanning microscopy (CLSM) was performed by measuring the reflected light intensity from a Zeiss 510 confocal with a HeNe 633 nm laser.

2.5. Scanning electrochemical microscopy (SECM)

Prior to SECM measurements, a montage image of a polished 4 mm × 4 mm area on an AM50 sand cast alloy sample was collected at 150× magnification using a Hitachi SU6600 Field Emission SEM. A complete map of the surface was produced by stitching the images using Image-Pro Plus 7.0®. SECM characterization was performed using an ElProScan 1 system (HEKA, Germany; bipotentiostat model PG340) by positioning a 25 μm Pt microelectrode over the alloy surface immersed in 1 mM FcMeOH solution (Sigma Aldrich) in ethylene glycol (Fisher Scientific). An approach curve was performed using feedback current from the FcMeOH mediator at an approach speed of 1 μm/s in order to position the microelectrode at a known distance of 10 μm from the surface. The microelectrode tip was polarized to 500 mV (vs. Ag/AgCl) and rastered at 5 μm/s over an area of interest (AOI). A 0.5 mm diameter (as drawn) Pt counter electrode (99.99%, Goodfellow Cambridge Limited, Huntingdon, England) and a Ag|AgCl quasi-reference wire electrode (fabricated as reported elsewhere [24] using a Ag wire of 1.0 mm diameter, annealed 99.99% from Goodfellow) were employed to record electrochemical data.

3. Results

3.1. AM50 alloy microstructure

The main microstructural constituents of the AM50 alloy are shown in the SEM micrograph in Fig. 1a, in which one of the many β-phase particles ($Mg_{17}Al_{12}$) is marked with a green arrow and an AlMn intermetallic with a red arrow. The compositions of individual phases were confirmed in the XEDS maps for Mg, Fig. 1b, which show the general distribution of Mg throughout the alloy matrix. The Al was present in both the β-phase and the intermetallic, Fig. 1c, with some enrichment in the network running between the β-phases corresponding to eutectic α-Mg. The Mn was present within the ten AlMn intermetallic particles in the imaged region, Fig. 1d.

3.2. Electrochemical behavior

The electrochemical behavior of the AM50 sand cast alloy was investigated in 3 mM NaCl in both NanoPure®H_2O and ethylene glycol. The chloride was added to enhance solution conductivity. Fig. 2 shows the E_{CORR} measured in 3 mM NaCl + H_2O (black) and 3 mM NaCl + ethylene glycol (red). In H_2O, E_{CORR} initially rose over the first 2 h of immersion from −1.56 V (vs. SCE) to −1.50 V (vs. SCE), and then increased slowly over the 24 h to −1.49 V (vs. SCE) accompanied by a number of small fluctuations. This final value was in the range expected for AM50 in aqueous chloride solutions [25]. In ethylene glycol E_{CORR} initially decreased from −1.05 V (vs. SCE) to −1.4 V (vs. SCE) over the first 2 h of immersion before increasing to a final steady-state value of ~−1.26 V (vs. SCE) after 24 h.

The PDP behavior of the alloy in both solutions is shown in Fig. 3. As expected the cathodic current at potentials less than E_{CORR} was considerably higher in H_2O than in ethylene glycol. In H_2O (black), once the net current became anodic at −1.45 V (vs. SCE) it increased (region I). For higher potentials the current increased sharply (region II). These features were typical of the behavior observed on this alloy [25] with an attempt to grow a partially protective film in region I followed by film breakdown and the onset of rapid dissolution in region II. In ethylene glycol (red), a similar initial event was observed with region I persisting to a potential of −1.10 V (vs. SCE). The subsequent increase in reactivity was minor, currents <1 μA/cm² being maintained before final film breakdown
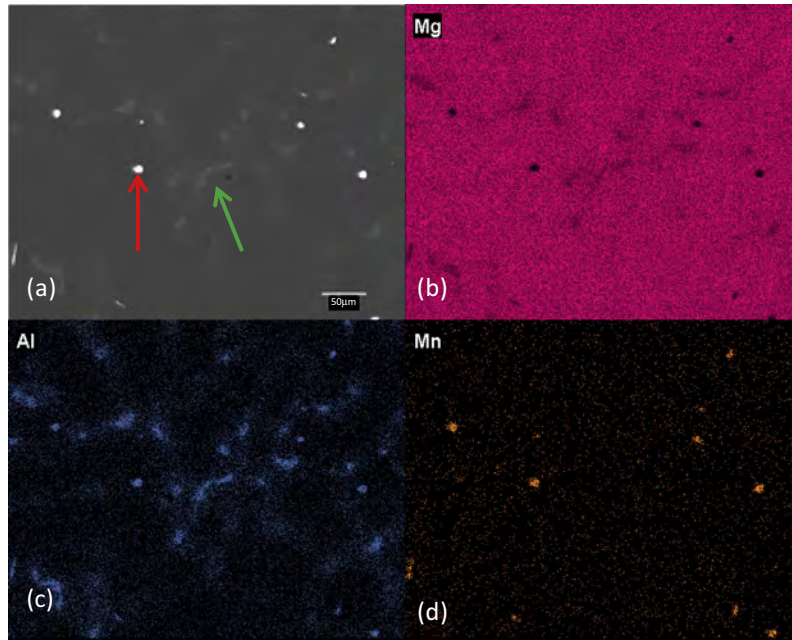
Fig. 1. The microstructure of a sand cast AM50 Mg alloy displaying the common microstructural features in (a) a SEM BSE image, and XEDS maps of (b) Mg, (c) Al, and (d) Mn. A β-phase structure is marked in the images with a green arrow and an AlMn intermetallic particle with a red arrow. (For interpretation of the references to color in this figure legend, the reader is referred to the web version of this article.)
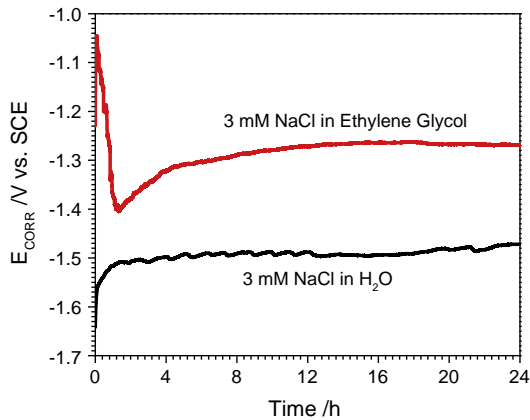

Fig. 2. Evolution of E_{CORR} measured on a sand cast AM50 Mg alloy in 3 mM NaCl solution in H_2O (black) and ethylene glycol (red). (For interpretation of the references to color in this figure legend, the reader is referred to the web version of this article.)
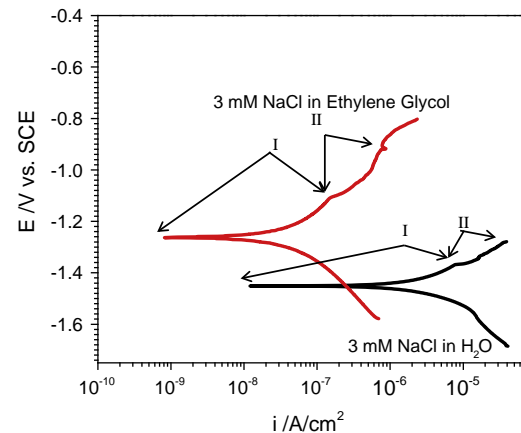

Fig. 3. PDP scans measured on a sand cast AM50 Mg alloy in 3 mM NaCl in ethylene glycol (red) and 3 mM NaCl in H_2O (black). (For interpretation of the references to color in this figure legend, the reader is referred to the web version of this article.)

for $E > \sim-0.80$ V (vs. SCE) (region II). Only at these high potentials did the current approach that observed in region I in H_2O when the surface is partially protected by corrosion product. For all potentials anodic to E_{CORR}, the currents measured in ethylene glycol were $\sim10^3$ less than those observed in H_2O. The solution conductivities were different for the two solutions, with the 3 mM NaCl in H_2O having a conductivity of 320 μS/cm and the 3 mM NaCl in ethylene glycol having a conductivity of 19.3 μS/cm. These conductivities correlated to iR drops of 13 mV in the aqueous environment and 20 mV in the glycol at the highest currents shown in the PDP scans.

The suppression of corrosion rate in ethylene glycol compared to H_2O was evident in the Nyquist plots in Fig. 4a, which were recorded after 20 h of immersion, and the Bode plots in Fig. 4b and c. In glycol, the E_{CORR} was −1.31 V (vs. SCE) and in H_2O −1.52 V (vs. SCE) prior to the EIS measurements. Extrapolation of these plots at the low frequency limit to the real axis yielded a

measure of the polarization resistance (R_P) which is inversely proportional to the corrosion rate. The value obtained for R_P in H_2O was nearly two orders of magnitude lower than that in ethylene glycol. The Nyquist plot recorded in H_2O exhibited two capacitive responses (I and II), the one at high frequencies being shown in the inset to Fig. 4a. The plot recorded in ethylene glycol exhibits two, possibly three capacitive responses (I, II and III) although whether or not the response at high frequencies (I) was a true response or a result of a combination of the dielectric properties of the solvent and the cell geometry remains to be determined. The characteristic frequency of the low frequency response in H_2O (0.5 Hz) was approximately the same as the characteristic frequency of the low frequency response in ethylene glycol, a possible indication that the signals arose from the same process at the electrode surface.
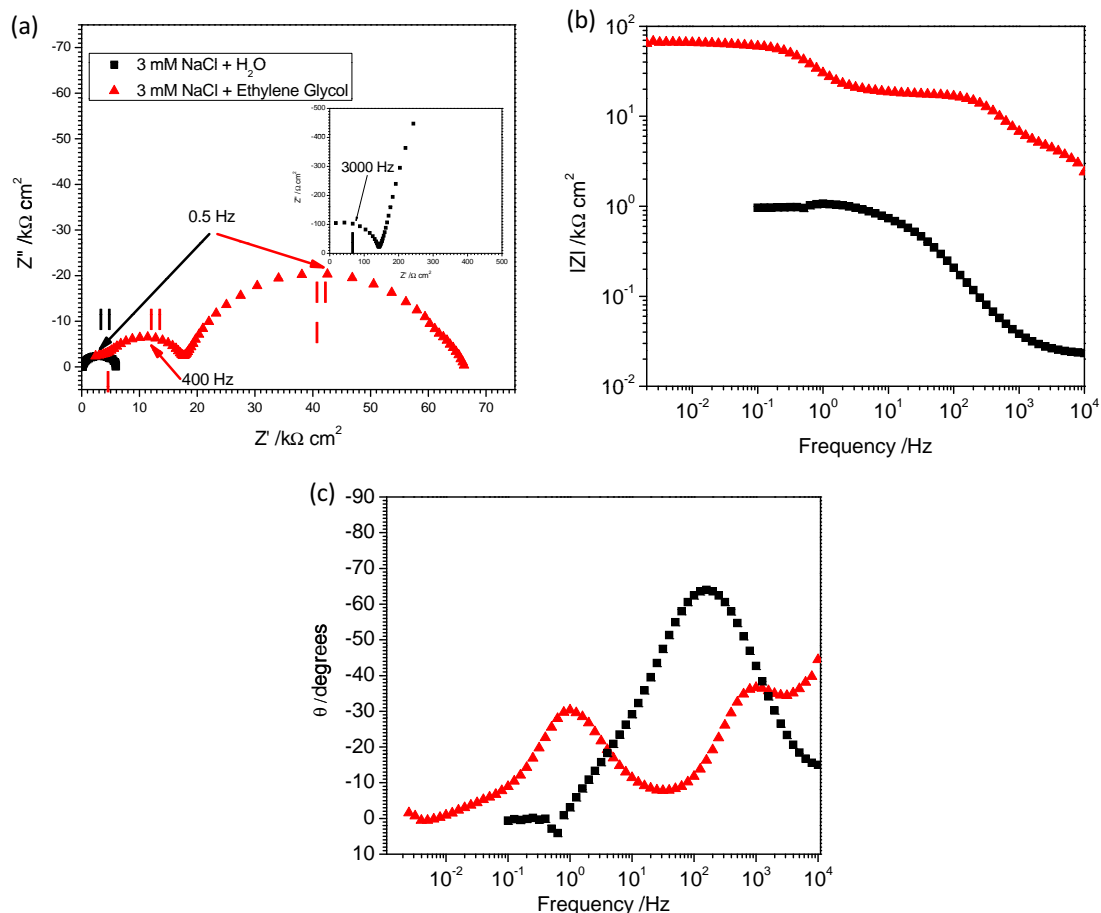
Fig. 4. (a) Nyquist plots recorded on a sand cast AM50 Mg alloy after 20 h exposure in 3 mM NaCl in H_2O (black) and ethylene glycol (red). Inset: magnification of the high frequency response in the H_2O solution: (b and c) show the corresponding Bode plots. (For interpretation of the references to color in this figure legend, the reader is referred to the web version of this article.)

3.3. Corrosion process control

The addition of H_2O to the ethylene glycol system has an intriguing effect, Fig. 5. The E_{CORR} of the sand cast AM50 alloy in the ethylene glycol solution initially increased to ∼−1.32 V (vs. SCE) and appeared to be approaching the same steady-state value previously observed (Fig. 2). On addition of 2 mL of H_2O (to 400 mL
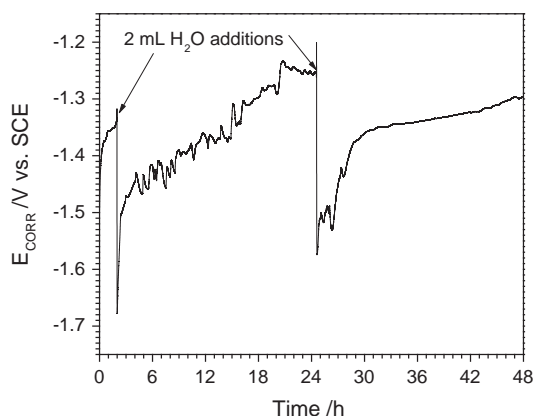

Fig. 5. Progression of E_{CORR} measured on a sand cast AM50 Mg alloy over a 48 h exposure period in 3 mM NaCl + ethylene glycol with 2 mL additions of H_2O made after 3 h and 25 h.

of ethylene glycol) after 2 h, E_{CORR} immediately dropped to −1.66 V (vs. SCE) before recovering to a value of ∼−1.45 V (vs. SCE) over the next 24 h, which was within the range expected in H_2O (Fig. 2). Subsequently, E_{CORR} increased steadily to a value of ∼−1.25 V (vs. SCE); i.e., a value close to that measured in ethylene glycol with no H_2O addition (Fig. 2). A second addition of 2 mL of H_2O induced a similar drop in E_{CORR} although the recovery over the subsequent 24 h was similar but not as complete as observed after the first H_2O addition.

Fig. 6a shows the E_{CORR} behavior of the sand cast AM50 alloy in 3 mM NaCl + ethylene glycol. Prior to the addition of 25 mL of H_2O (to 400 mL of ethylene glycol) after 2 h, (a larger addition of H_2O was used to ensure that the effect was sustained for the duration of EIS measurements) E_{CORR} was more negative than measured in the previous experiment (Fig. 2). Since the E_{CORR} measured in H_2O is significantly lower than the E_{CORR} in ethylene glycol (Fig. 2), and upon the addition of H_2O to ethylene glycol a decrease in E_{CORR} was observed, the lower E_{CORR} seen in Fig. 6a suggested that, in this case, the ethylene glycol contained more H_2O than in the previous experiment, a likely result of its hygroscopic nature.

This sensitivity to H_2O content of the ethylene glycol was further indicated by a comparison of the impedance spectra recorded in the two experiments, the overall impedance of the alloy/solution interface being considerably lower in this second experiment. This can be appreciated by a comparison of the Nyquist plots in Figs. 4 and 6b. In the first experiment in which the H_2O content of the ethylene glycol appeared to be low, extrapolation of the low frequency
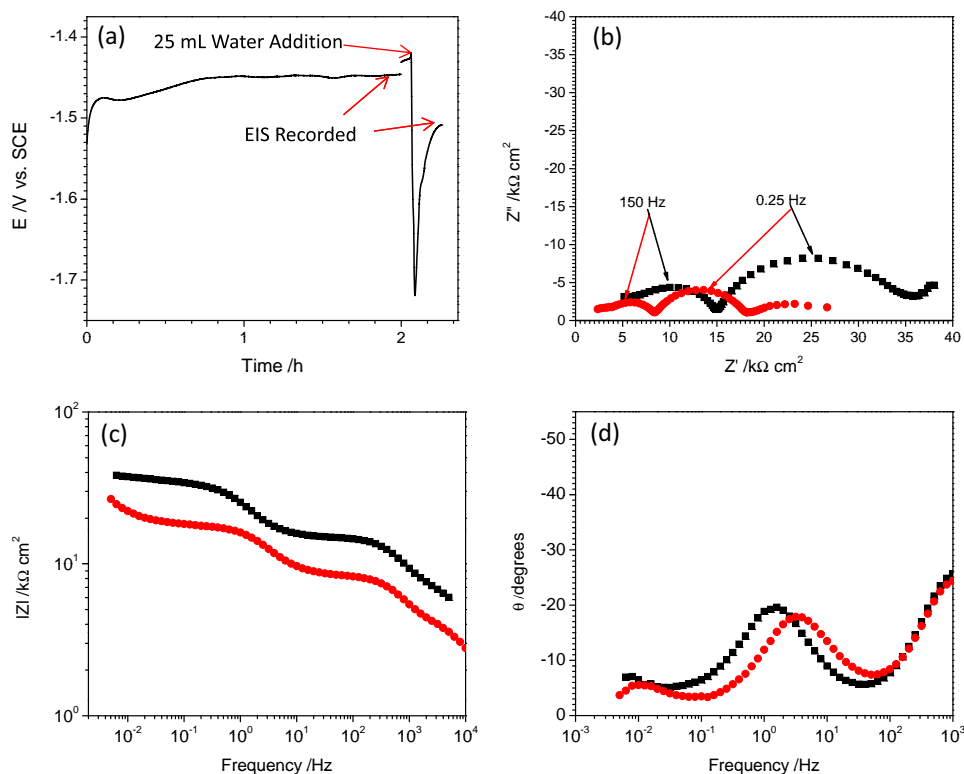
Fig. 6. (a) Progress of E_{CORR} measured on a sand cast AM50 Mg alloy in 3 mM NaCl + ethylene glycol. EIS measurements were made just before and after the addition of 25 mL of H_2O at ~2 h: (b) Nyquist plots, and (c and d) Bode plots recorded just before (black) and after (red) H_2O addition. (For interpretation of the references to color in this figure legend, the reader is referred to the web version of this article.)

response to the real axis would yield an R_P value of ~67 kΩ cm^2 compared to ~35 kΩ cm^2 in this second experiment.

In the second experiment (Fig. 6a), EIS measurements were performed just prior to and following the addition of H_2O, Fig. 6b–d. Comparison of the characteristic frequencies for the two capacitive responses observed showed they were the same for both spectra and similar to the spectrum in ethylene glycol in Fig. 4. This similarity in response was confirmed by the Bode plots in Fig. 6c and d which showed only a small change in both time constants after H_2O addition. The key difference was in the overall impedance which decreased by a factor of ~2 on the addition of H_2O. In both cases the spectra showed a low frequency response at <10^{-1} Hz which suggested some contribution from diffusion, most likely of H_2O in the glycol.

3.4. Microstructure behavior in ethylene glycol

Our previous results show that AlMn intermetallic particles can act as cathodes in the corrosion of AM50 alloys in saline aqueous environments [26–27], and that the presence of an accumulated dome of corrosion product (predominantly $Mg(OH)_2$) is evidence of this function [27]. This corrosion product is formed as a consequence of the alkalinity generated by H_2O reduction to H_2 gas on the intermetallic particles which leads to the precipitation of soluble Mg^{2+} transported to this location from adjacent anodically dissolving areas of the surface. Fig. 7a shows a backscattered SEM image of the freshly polished alloy. The β-phase network was clearly visible as irregularly shaped light strips in the image, and a large bright AlMn intermetallic was visible in the top right corner. A magnified image of this particle is shown in Fig. 7c. Fig. 7b and d show the same particle after 72 h of exposure to 3 mM NaCl + ethylene glycol solution. The low magnification image, Fig. 7b showed slight corrosion damage of the α-Mg matrix had

occurred as indicated by the green arrow. No observable change in the β-phase network was visible. The AlMn intermetallic particle, which appears dark in Fig. 7b, had accumulated a deposit of corrosion product, Fig. 7d, clearly indicating its function as a cathode actively supporting the corrosion of the surrounding α-matrix.

3.5. Scanning electrochemical microscopy in ethylene glycol

Fig. 8 shows a 4 mm × 4 mm area of the surface of the AM50 alloy which was montage imaged to identify the area to be mapped by SECM. This imaging process allows us to identify an area within which we could cross-correlate the SECM measurements with the distribution of microstructural features in the surface. The selected AOI for SECM measurements is marked with the red box.

In SECM experiments, the sample was exposed to a 1 mM solution of FcMeOH in ethylene glycol. A cyclic voltammogram recorded with a 25 μm Pt microelectrode in this solution at a scan rate of 10 mV/s is shown in Fig. 9a. A steady state current (for the oxidation FcMeOH → FcMeOH$^+$ + e$^-$) was observed for E > 400 mV (vs. Ag/AgCl) and 500 mV (vs. Ag/AgCl) was selected as the microelectrode potential during SECM measurements. To position the probe at a 10 μm tip to substrate distance, feedback current probe approach curves with an approach speed of 1 μm/s were recorded, Fig. 9b, at the locations marked 1 and 2 in Fig. 10a.

Following positioning, the microelectrode was rastered over a 500 μm × 500 μm area at a scan rate of 5 μm/s with a potential of 500 mV (vs. Ag/AgCl) applied to the tip while keeping the alloy surface at E_{CORR}. The SECM map recorded, Fig. 10a, showed clearly distinguishable regions with the microelectrode tip current varying between 300 and 400 pA.

The approach curve recorded at location 2 yields slightly negative feedback behavior indicating low reactivity while that at location 1 yields slightly positive feedback behavior Fig. 9b. Due to a
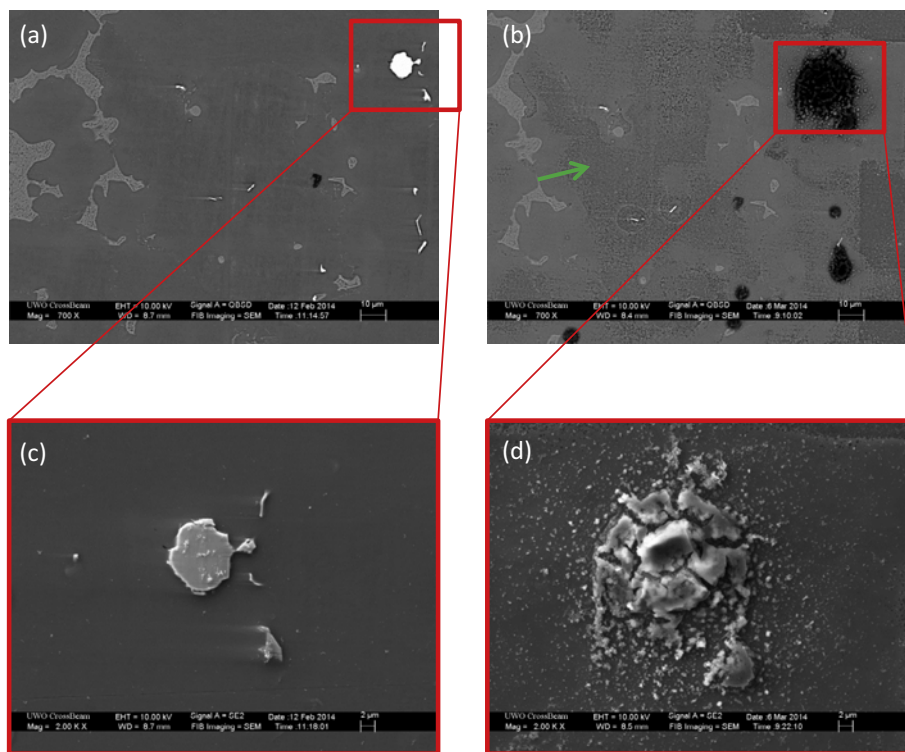
Fig. 7. Back-scattered SEM micrographs of a graphite cast AM50 Mg alloy (a) polished surface, and (b) following 72 h in 3 mM NaCl in ethylene glycol with the green arrow denoting a region of accumulated corrosion damage: (c) an AlMn intermetallic marked in (a), (d) the intermetallic following exposure having collected a mass of corrosion product. (For interpretation of the references to color in this figure legend, the reader is referred to the web version of this article.)
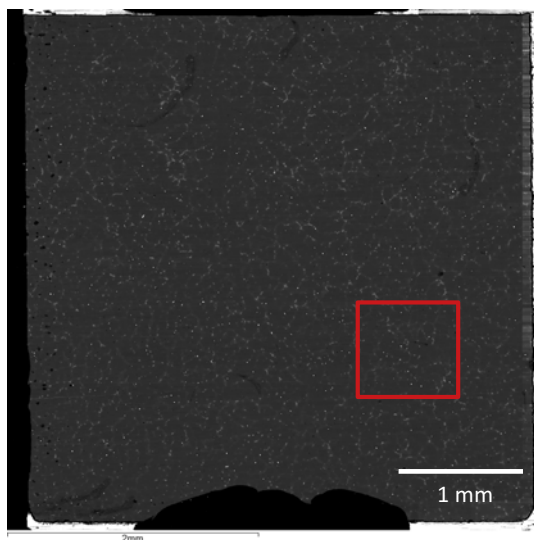

Fig. 8. Montage SEM map recorded on a sand cast AM50 Mg alloy. The red box shows the location chosen for SECM measurements. (For interpretation of the references to color in this figure legend, the reader is referred to the web version of this article.)

regeneration of the oxidized mediator at the microelectrode tip, FcMeOH$^+$ diffused toward the surface being reduced back to FcMeOH. Heterogeneous rate constants (k_o) were extracted to quantify the rate at which the mediator was regenerated at these locations. By fitting the approach curves to an analytical approximation [28], values of $k_1 = 1.02 \times 10^{-2}$ cm/s and $k_2 = 3.13 \times 10^{-3}$ cm/s were obtained, clearly demonstrating the difference in reactivity

between these locations. For comparison, the analytical approximation for full positive (diffusion controlled reactivity) and negative (no reactivity on an insulating surface) feedback are also shown, plots (I) and (II) in Fig. 9b, respectively.

Fig. 10b shows the SECM image (Fig. 10a) superimposed on the SEM image of the polished AM50 sample with the red arrow highlighting two AlMn intermetallic particles and a circular arrangement of β-phase. These overlaid images show that the reactive areas (faster kinetics in the probe approach curve) were associated with the α-Mg locations on the surface and the regions of low reactivity (slower kinetics) with β-phase ligaments and surrounding eutectic regions.

Following the SECM experiment the AOI was re-examined and both BSE and SE micrographs are shown in Fig. 11a and b, respectively. To assist in image comparison, the same two AlMn intermetallic particles identified in Fig. 10b are indicated by the red arrow. The SE image in Fig. 11b showed the collection of some corrosion product (identified as the slightly lighter regions) on the α-Mg areas of the surface.

The 3D CLSM image in Fig. 12a shows an area of an AM50 alloy surface imaged after exposure to ethylene glycol solution for 24 h, and Fig. 12b the AOI imaged by SECM after exposure to the ethylene glycol + FcMeOH solution. The red arrow again identifies the location of the two Al–Mn structures highlighted in Figs. 10 and 11. It is clear from these images that the surface was much more extensively damaged after exposure to the ethylene glycol containing FcMeOH than it is in the ethylene glycol alone. The darker areas in the CLSM image in Fig. 12b coincided with the corrosion product-covered α-Mg areas (dark since the laser beam was scattered rather than reflected) and the lighter areas with the less corroded β-phase/eutectic skeletal-like structure. Comparison of this CLSM image with the overlaid SEM/SECM map (Fig. 10b) confirmed that FcMeOH$^+$ was active in corroding the alloy surface and that it was consumed primarily at α-Mg locations.
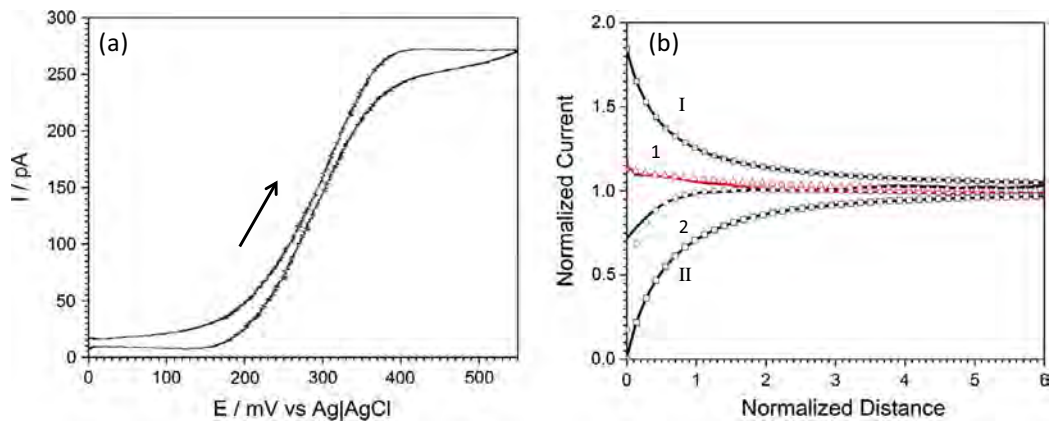
Fig. 9. (a) A cyclic voltammogram recorded on a Pt microelectrode in 1 mM FcMeOH in ethylene glycol at 10 mV/s, the arrow represents the initial scan direction: (b) approach curves recorded at locations 1 and 2 labeled in Fig. 10a (△ and ○). I and II show the calculated approach curves for a diffusion limited reaction and an insulating unreactive surface, respectively.
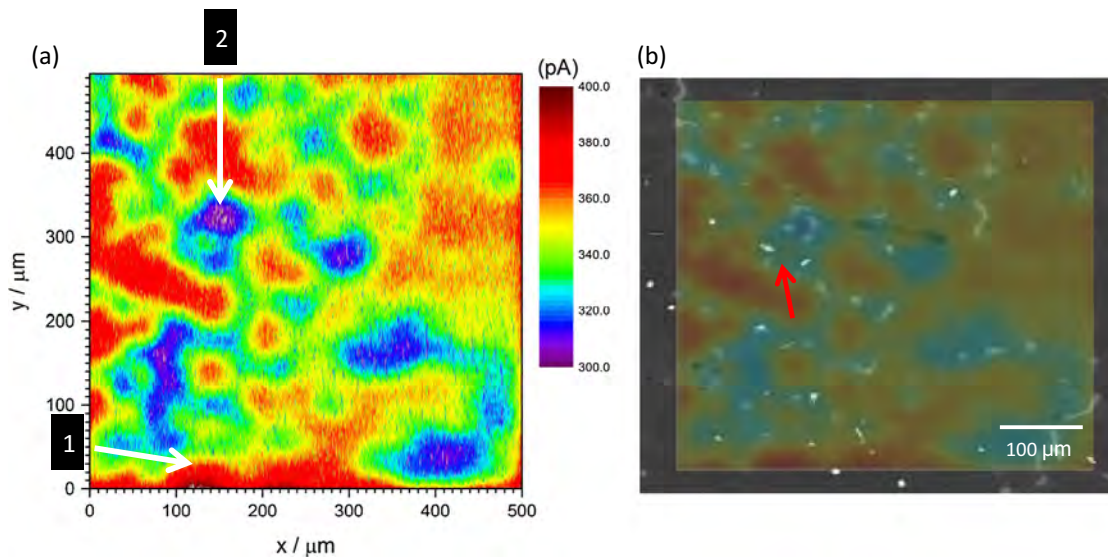

Fig. 10. (a) SECM map recorded on a sand cast AM50 Mg alloy in 1 mM FcMeOH + ethylene glycol using a Pt microelectrode polarized at 500 mV located 10 μm above the surface and rastered across the surface at 10 μm/s: (b) an overlay of SEM and SECM images of the same area. The red arrow indicates two Al–Mn particles used to relocate this area in the images. (For interpretation of the references to color in this figure legend, the reader is referred to the web version of this article.)
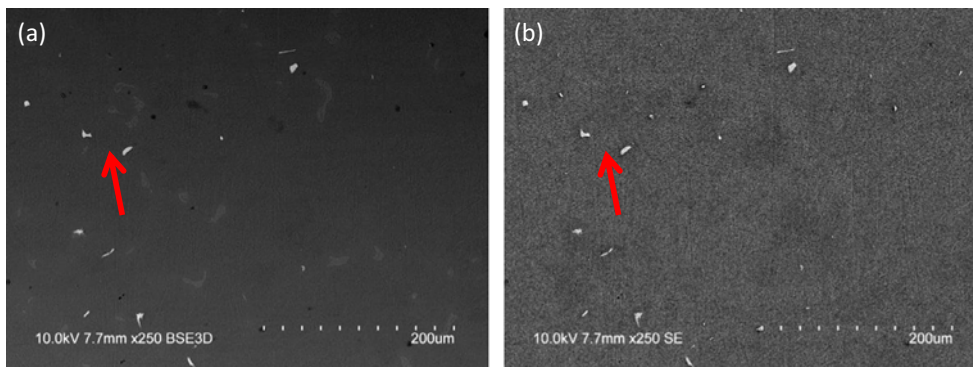

Fig. 11. (a) SEM BSE micrograph of the AOI on the sand cast AM50 Mg alloy following the SECM measurement shown in Fig. 10; and (b) SEM SE micrograph of the AOI. Red arrows identify the same AlMn intermetallic particles in each micrograph. (For interpretation of the references to color in this figure legend, the reader is referred to the web version of this article.)
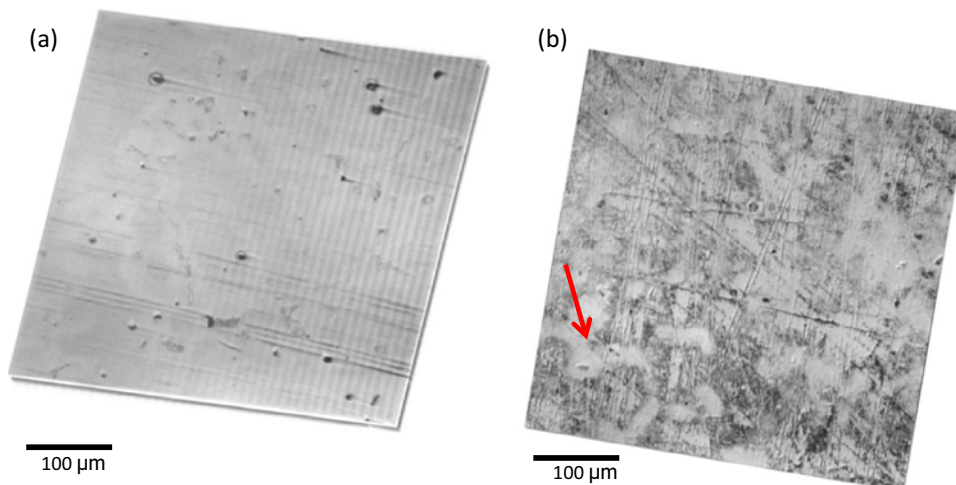
Fig. 12. 3D CLSM micrographs of (a) AM50 Mg alloy exposed for 24 h in ethylene glycol and (b) the AOI on the AM50 Mg alloy following the SECM measurement in Fig. 10 showing slight damage accumulation in regions which generated positive feedback current in the SECM experiment; The red arrow shows the location of the two Al–Mn intermetallic particles highlighted with arrows in Fig. 11.

4. Discussion

In the aqueous corrosion of pure Mg or Mg alloys, the oxidation of α-Mg regions is coupled with H_2O reduction, the two reactions occurring at equal rates, as demonstrated recently by a multitude of techniques [29,30]. A detailed summary of the overall corrosion mechanism in aqueous environments leading to $Mg(OH)_2$ deposits has recently been published [31]. The cathodic half reaction occurs predominantly on the most kinetically active locations, not necessarily the most noble with respect to the Mg matrix, (ie. impurities, intermetallic particles, secondary phases) [32] and, if these sites are limited, the corrosion rate is reduced. This can be achieved through alloy purification [33] or the inclusion of cathodically inept secondary phases [34]. The goal of this project was to demonstrate whether or not the corrosion of a Mg alloy, which proceeds rapidly in aqueous solution with the production of copious amounts of H_2 [35,36], could be slowed down in ethylene glycol without changing the progression of damage morphology or changing the roles played by the individual microstructural features, thereby allowing the reaction to be followed using high resolution electrochemical microscopic techniques.

In ethylene glycol, which will contain only small amounts of H_2O, the cathodic reactions have been reported to be oxygen reduction and the less likely reduction of the ethylene glycol [37]. However, the large positive shift in E_{CORR} (Fig. 2) and $\sim10^2$ drop in cathodic current in the PDP scans (Fig. 3) on switching from an aqueous solution to the ethylene glycol solution suggest that H_2O, even when present in small amounts in ethylene glycol, was the dominant cathodic reagent. This appeared to be confirmed by the influence of adding small amounts of H_2O on E_{CORR} and the EIS spectra. The immediate drop in E_{CORR} (Fig. 5) confirmed the spontaneous effect of H_2O on the corrosion process. The subsequent rise in E_{CORR} over a period of ~22 h to the value expected prior to H_2O addition, suggested the H_2O was being consumed in the corrosion process. A subsequent addition of H_2O led to similar behavior.

A possibility on switching from H_2O to ethylene glycol, when the conductivity of the solution was considerably lower, is that the lower conductivity was the primary influence on the corrosion process, not a distinct suppression of the cathodic kinetics due to a lack of H_2O. However, the iR drops in the electrochemical measurements were minimal for the potential ranges investigated, and any effect of the solution conductivity would be in the ability of the cathodes in the alloy to microgalvanically couple to the α-Mg matrix.

This influence of changing from H_2O to ethylene glycol on the impedance of the alloy/solution interface is clear in Fig. 4, the polarization resistance (estimated by extrapolating the spectra to the zero frequency limit) increasing by approximately two orders of magnitude. Despite this change, the Nyquist plots in aqueous solution and ethylene glycol both exhibited two capacitative responses, comparable features to previously reported systems in H_2O and ethylene glycol [5,38]. In aqueous systems, the high frequency response has been attributed to the charge transfer process ($Mg \rightarrow Mg^{2+}$) and film capacitance at the alloy surface, and the lower frequency response to the diffusion of Mg^{2+} through the thickening $MgO/Mg(OH)_2$ corrosion product film [5]. If these assignments are accepted, then the Nyquist plots show the characteristic frequency for the charge transfer process (an indication of the time constant of the response) was considerably larger in H_2O (~3000 Hz) than in ethylene glycol (~400 Hz); i.e., the kinetics of the initial charge transfer process were considerably faster in H_2O. By contrast the characteristic frequencies for the lower frequency response were approximately the same despite the large increase in overall resistance.

The significant increase in E_{CORR} combined with a decrease in corrosion rate indicated by the impedance measurements was consistent with a combination of suppressed cathodic kinetics and the formation of a more coherent protective film. This claim was clearly supported by the polarization curves which show a very significant suppression of both the cathodic and anodic kinetics. The considerably larger influence (of switching from H_2O to ethylene glycol) on the anodic reaction compared to the cathodic reaction, apparent in the PDP scans (Fig. 3), suggested that lowering the amount of available H_2O can lead to improved cohesiveness and protectiveness of the anodically-formed film.

This claim, that the protectiveness of the corrosion product film was improved on switching from H_2O to ethylene glycol, was also supported by the impedance data. When E_{CORR} in ethylene glycol was high in the first experiment (-1.26 V (vs. SCE), Fig. 2), the impedances associated with both the interfacial charge transfer (II in Fig. 4a) and the film properties (III in Fig. 4a) were substantially increased. In the second experiment, when the presence of more H_2O was suspected, E_{CORR} was considerably more negative (~1.45 V (vs. SCE), Fig. 6) and the two impedances considerably lower. That H_2O content is the primary feature controlling the

corrosion rate is then confirmed by the reduction in both imped-
ances on the further addition of H_2O (Fig. 6). The electrochemical
data thus supports two effects of changing from an aqueous elec-
trolyte to ethylene glycol; (1) a reduction in the kinetics of the
cathodic half reaction by limiting access to H_2O as an oxidant,
and (2) an improvement in the properties of the film formed on
the alloy surface.

The SEM micrographs in Fig. 7 confirmed that corrosion in eth-
ylene glycol proceeded via the same microstructural processes
observed for the corrosion of this alloy in aqueous chloride solu-
tions, but with a much lower rate of damage accumulation. The
graphite cast AM50 alloy used in this exposure showed identical
corrosion damage morphology, albeit on a smaller scale, to that
observed on the sand cast AM50 alloy [25]. Damage generally
accumulated on the α-Mg grains (Fig. 7b) with the Al–Mn interme-
tallic particles acting as microgalvanically-coupled cathodes
(Fig. 7d) [26,27]. The extent of damage to the α-Mg grains was
minimal after 72 h of exposure consistent with SEM observations
(see Fig. 11b below) that these areas, while corroded, were uni-
formly covered with a thin layer of corrosion product. In addition,
the β-phase regions and the areas of surrounding eutectic
remained uncorroded, which was also observed after corrosion in
aqueous solutions [26]. In the case of the eutectic regions, this
was attributed to their higher Al content compared to the core of
the α-matrix which led to their protection by the enrichment of
Al at the alloy/oxide interface [26].

With the corrosion rate suppressed in this manner, as demon-
strated by the electrochemical measurements, the H_2 production
was also suppressed making it possible to map the corrosion pro-
cess using SECM, distinct differences in feedback current being
observed on the different microstructural regions on the surface.
The observed spatial variations in current could have arisen from
two scenarios; (1) the migration of the $FcMeOH^+$ species from
the microelectrode tip to a region based on the Volta potential of
that region, or (2) the function of $FcMeOH^+$ as an oxidant involved
in the corrosion of the α-Mg when generated at the microelectrode
tip. As discussed above, the alloy surface contained a number of
phases for which different average Volta potentials have been
reported relative to the α-Mg matrix phase, i.e., $AlMn + 257$ mV,
β-phase $+ 152$ mV [39]. These differences could cause the preferen-
tial migration of the $FcMeOH^+$ to the less noble regions, and would
lead to an SECM map in which the relative feedback currents
reflected the Volta potential differences. However, if such a contri-
bution to the tip current existed, it was minimal since no difference
in current resolution was detected between the β-phase and the
AlMn in the system, the regions surrounding these features all
showing low currents, Fig. 10.

The CLSM evidence in Fig. 12 confirmed that the presence of
FcMeOH was driving a slow but significant corrosion process, an
influence requiring further investigation. However, as opposed to
H_2O, which is reduced predominantly on features such as the AlMn
particles leading to corrosion of the α-matrix by microgalvanic
coupling, the generated $FcMeOH^+$ at the microelectrode tip was
reduced at the most anodically reactive locations. According to
the SECM and SEM maps in Fig. 10, this order of reactivity is

α-Mg matrix $>$ Al-containing eutectic $>$ β-phase/Al$-$Mn

In this regard, SECM provided a map of the anodic reactivity of the
surface. While this may be intuitively surprising since $FcMeOH^+$ is a
localized cathodic reagent, it most likely reflected two features: (i)
the rapid kinetics of the $FcMeOH^+$/FcMeOH couple which dictated
that reduction occurred on the most conductive location rather than
on a catalytic secondary phase location; and (ii) the more limited
range of microgalvanic coupling possible in the less conductive eth-
ylene glycol solution. In this somewhat surprising manner, SECM
using an $FcMeOH^+$ mediator gave an excellent indication of the

corrosivity of individual surface locations. A comparison of the
SECM map to the CLSM image obtained for the corrosion of this
alloy in an aqueous system confirmed that the corrosion damage
morphology and roles played by the microstructural features, while
muted by the reduced conductivity in ethylene glycol, are the same
as in H_2O [26].

5. Conclusions

The corrosion of a sand cast AM50 Mg alloy was studied in eth-
ylene glycol with and without added H_2O. A combination of elec-
trochemical and microscopic investigations showed similar
corrosion processes occurred in ethylene glycol as in H_2O but con-
siderably slower. Experiments in which H_2O was added to the eth-
ylene glycol demonstrated that H_2O is the key cathodic reagent in
this solvent, not oxygen reduction or reduction of the ethylene gly-
col. By slowing the corrosion process and avoiding excessive H_2
production, it was possible to map the corrosion response of the
alloy by SECM using the redox mediator FcMeOH. The $FcMeOH^+$
produced at the microelectrode tip acted as an oxidant at the alloy
surface. Due to its rapid electron transfer kinetics, the $FcMeOH^+$
was reduced on the most conducting surface locations to yield a
map of the spatial distribution of anodic reactivity. The reactivity
of the different surface phases were found to be in the order α-
Mg matrix $>$ Al-containing eutectic $>$ β-phase/Al–Mn intermetallic
confirming that the corrosion process of the alloy is the same in
ethylene glycol as in H_2O. Reducing the corrosion rate of Mg alloys,
without a large alteration in the roles played by the microstruc-
tural features, through solvent selection presents a potentially
valuable approach to analyzing the corrosion processes on Mg
alloys with increased resolution and detail.

References

[1] J. Hirsch, T. Al-Samman, Superior light metals by texture engineering:
Optimized aluminum and magnesium alloys for automotive applications,
Acta Mater. 61 (2013) 818–843.
[2] S. Mathieu, C. Rapin, J. Steinmetz, A corrosion study on the main constituent
phases of AZ91 magnesium alloys, Corros. Sci. 45 (2003) 2741–2755.
[3] H. Matsubara, Y. Ichige, K. Fujita, H. Nishiyama, K. Hodouchi, Effect of impurity
Fe on corrosion behavior of AM50 and AM60 magnesium alloys, Corros. Sci. 66
(2013) 203–210.
[4] G. Baril, C. Blanc, M. Keddam, N. Pebere, Local electrochemical impedance
spectroscopy applied to the corrosion behaviour of an AZ91 magnesium alloy,
J. Electrochem. Soc. 150 (2003) B488–B493.
[5] G. Galicia, N. Pebere, B. Tribollet, V. Vivier, Local and global electrochemical
impedance applied to corrosion behaviour of an AZ91 magnesium alloy,
Corros. Sci. 51 (2009) 1789–1794.
[6] D. Bengtsson Blucher, J.E. Svensson, L.G. Johansson, M. Rohwerder, M.
Stratmann, Scanning Kelvin probe force microscopy: A useful tool for
studying atmospheric corrosion of MgAl alloys in-situ, J. Electrochem. Soc.
151 (2004) B621–B626.
[7] M. Jonsson, D. Thierry, N. LeBozec, The influence of microstructure on the
corrosion of AZ91D studied by scanning Kelvin probe force microscopy and
scanning Kelvin probe, Corros. Sci. 48 (2006) 1193–1208.
[8] G. Williams, H.N. McMurray, Localized corrosion of magnesium in chloride
containing electrolyte studied by a scanning vibrating electrode technique, J.
Electrochem. Soc. 155 (2008) C340–C349.
[9] G. Williams, N. Birbilis, H.N. McMurray, The source of hydrogen evolved from a
magnesium anode, Electrochem. Commun. 36 (2013) 1–5.
[10] K.B. Deshpande, Experimental investigation of galvanic corrosion: comparison
between SVET and immersion techniques, Corros. Sci. 52 (2010) 2819–2826.

[11] Z.P. Cano, M. Danaie, J.R. Kish, J.R. McDermid, G.A. Botton, G. Williams, Physical characterization of cathodically activated corrosion filaments on magnesium alloy AZ31, Corrosion (2014), http://dx.doi.org/10.5006/1384.

[12] D. Trihn, P. Dauphin Ducharme, U.M. Tefashe, J.R. Kish, J. Mauzeroll, Influence of edge effects on local corrosion rate of magnesium alloy/mild steel galvanic couple, Anal. Chem. 84 (2012) 9899–9906.

[13] S.V. Lamaka, O.V. Karavai, A.C. Bastos, M.L. Zheludkevich, M.G.S. Ferreira, Monitoring local spatial distribution of Mg^{2+}, pH and ionic currents, Electrochem. Commun. 10 (2008) 259–262.

[14] J. Izquierdo, L. Nagy, I. Bitter, R. Souto, G. Nagy, Potentiometric scanning electrochemical microscopy for the characterization of the electrochemical behaviour of magnesium-based materials, Electrochim. Acta 87 (2013) 283–293.

[15] R.M. Souto, A. Kiss, J. Izquierdo, L. Nagy, I. Bitter, G. Nagy, Spatially resolved imaging of concentration distributions on corroding magnesium based materials exposed to aqueous environments by SECM, Electrochem. Commun. 26 (2013) 25–28.

[16] W. Liu, F. Cao, Y. Xia, L. Chang, J. Zhang, Localized corrosion of magnesium alloys in NaCl solutions explored by scanning electrochemical microscopy in feedback mode, Electrochim. Acta 132 (2014) 377–388.

[17] S.S. Jamali, S.E. Moulton, D.E. Tallman, M. Forsyth, J. Weber, G.G. Wallace, Applications of scanning electrochemical microscopy for local characterization of AZ31 surface during corrosion in a buffered media, Corros. Sci. 86 (2014) 93–100.

[18] S. Thomas, J. Izquierdo, N. Birbilis, R.M. Souto, Possibilities and limitations of scanning electrochemical microscopy of Mg and Mg alloys, Corrosion, in press, 2014, http://dx.doi.org/10.5006/1483.

[19] U.M. Tefashe, M.E. Snowden, P. Dauphin Ducharme, M. Danaie, G.A. Botton, J. Mauzeroll, Local flux of hydrogen from magnesium alloy corrosion investigated by scanning electrochemical microscopy, J. Electroanal. Chem. 720–721 (2014) 121–127.

[20] P. Dauphin-Ducharme, R.M. Asmussen, U.M. Tefashe, M. Danaie, W.J. Binns, P. Jakupi, G. Botton, D. Shoesmtih, J. Mauzeroll, Local hydrogen fluxes correlated to microstructural features of a corroding sand cast AM50 magnesium alloys, J. Electrochem. Soc. 161 (2014) C557–C564.

[21] A.M. Fekry, M.Z. Fatayerji, Electrochemical corrosion behaviour of AZ91D in ethylene glycol, Electrochim. Acta 54 (2009) 6522–6528.

[22] G. Song, D. St, John, Corrosion behaviour of magnesium in ethylene glycol, Corros. Sci. 46 (2004) 1381–1399.

[23] L. Wang, T. Zhou, J. Liang, Corrosion and self healing behaviour of AZ91D magnesium alloy in ethylene glycol/water solutions, Mater. Corros. 63 (2012) 713–719.

[24] T.J. Smith, K.J. Stevenson, Handbook of Electrochemistry, in: C.G. Zoski (Ed.), Elsevier, Amsterdam, 2007, pp. 73–110.

[25] R.M. Asmussen, W. Binns, P. Jakupi, D.W. Shoesmith, The microstructural influences on the corrosion of magnesium alloys, J. Electrochem. Soc. 161 (2014) C501–C508.

[26] R.M. Asmussen, P. Jakupi, M. Danaie, G. Botton, D.W. Shoesmith, Tracking the corrosion of magnesium sand cast AM50 alloys in chloride environments, Corros. Sci. 75 (2013) 114–122.

[27] M. Danaie, R.M. Asmussen, P. Jakupi, D.W. Shoesmith, G. Botton, The cathodic behaviour of Al–Mn precipitates during atmospheric and saline aqueous corrosion of a sand-cast AM50 alloy, Corros. Sci. 83 (2014) 299–309.

[28] R. Cornut, S. Griveau, C. Lefrou, Accuracy study on fitting procedure of kinetics SECM feedback experiments, J. Electroanal. Chem. 650 (2010) 55–61.

[29] A.D. King, N. Birbilis, J.R. Scully, Accurate electrochemical measurement of magnesium corrosion rates; a combined impedance, mass-loss and hydrogen collection study, Electrochim. Acta 121 (2014) 394–406.

[30] L. Rossrucker, K.J.J. Mayrhofer, G.S. Frankel, N. Birbilis, Investigating the real time dissolution of Mg using online analysis by ICP-MS, J. Electrochem. Soc. 161 (2014) C115–C119.

[31] S. Thomas, N.V. Medhekar, G.S. Frankel, N. Birbilis, Corrosion mechanism and hydrogen evolution on Mg, Curr. Opin. Solid State Mater. Sci. (2014), http://dxdoi.org/10.1016/j.cossms.2014.09.005.

[32] A.D. Sudholz, N.T. Kirkland, R.G. Buchheit, N. Birbilis, Electrochemical properties of intermetallic phases and common impurity elements in magnesium alloys, Electrochem. Sol. State Lett. 14 (2011) C5–C7.

[33] J.D. Hanawalt, C.E. Nelson, J.A. Peloubet, Corrosion studies of magnesium and its alloys, Trans. AIME 147 (1942) 273–299.

[34] N. Birbilis, G. Williams, K. Gusieva, A. Samaniego, M.A. Gibson, H.N. McMurray, Poisoning the corrosion of magnesium, Electrochem. Commun. 34 (2013) 295–298.

[35] G.S. Frankel, A. Samaniego, N. Birbilis, Evolution of hydrogen at dissolving magnesium surfaces, Corros. Sci. 70 (2013) 104–111.

[36] N.T. Kirkland, G. Williams, N. Birbilis, Observations of the galvanostatic dissolution of pure magnesium, Corros. Sci. 65 (2012) 5–9.

[37] G.A. Zhang, L.Y. Xu, Y.F. Cheng, Mechanistic aspects of electrochemical corrosion of aluminum alloy in ethylene glycol–water solution, Electrochim. Acta 53 (2008) 8245–8252.

[38] E. Slavcheva, G. Petkova, P. Andreev, Inhibition of corrosion of AZ91 magnesium alloy in ethylene glycol solution in presence of chloride anions, Mater. Corros. 56 (2005) 83–87.

[39] F. Andreatta, I. Apachitei, A.A. Kodentsov, J. Dzwonczyk, J. Dusczczyk, Volta potential of second phase particles in extruded AZ80 magnesium alloy, Electrochim. Acta 51 (2006) 3551–3557.